**Additional file 2**

**Fig. S1: Diurnal variation in cfDNA levels and deconvolution validation**

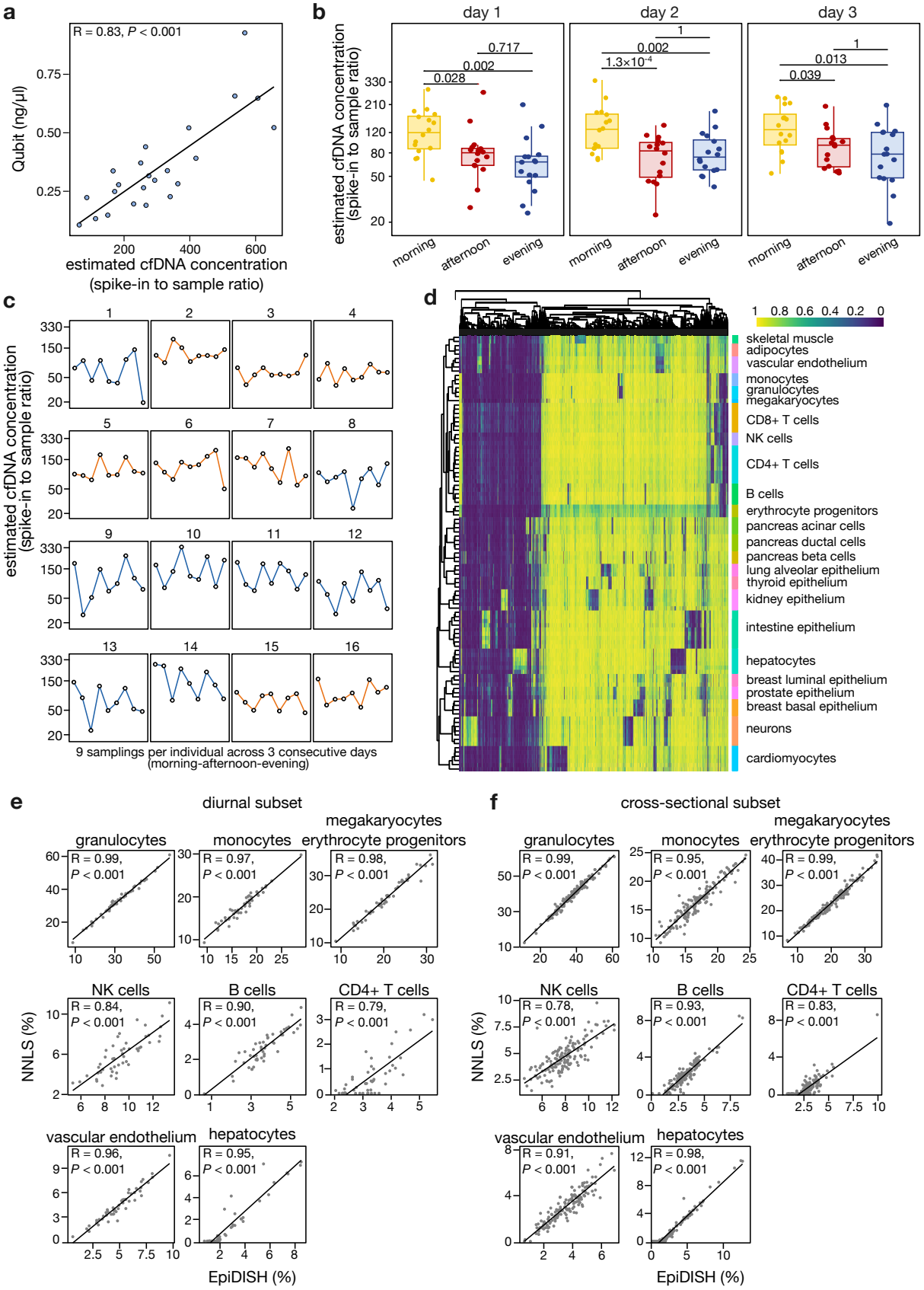


**a,** Pearson correlation between cfDNA concentrations measured by Qubit post-extraction (*n* = 23 samples) and estimated concentrations based on spiked-in lambda viral vector DNA (Methods). **b**, Estimated cfDNA concentration levels across timepoints (morning, afternoon

and evening) over three consecutive sample days. **c**, Individual estimated cfDNA concentration trajectories for male (blue) and female (orange) participants in the diurnal cohort across the three sampling days. **d**, Heatmap of marker CpG methylation ($n$ = 5,699) used for cell type deconvolution of 24 cell types. **e-f**, Pearson correlation between cell type proportion estimates from EpiDISH and non-negative least squares (NNLS)-based cfDNA deconvolution in subsets of the diurnal (**e**; day 1, $n$ = 48) and cross-sectional (**f**; year 1, $n$ = 144) cohorts. *P* values by Pearson correlation (a, e, f), repeated measures ANOVA for all sampling days combined, followed by pairwise t-test on each individual day (b).

**Fig. S2: Diurnal variation in cfDNA composition and fragment length**

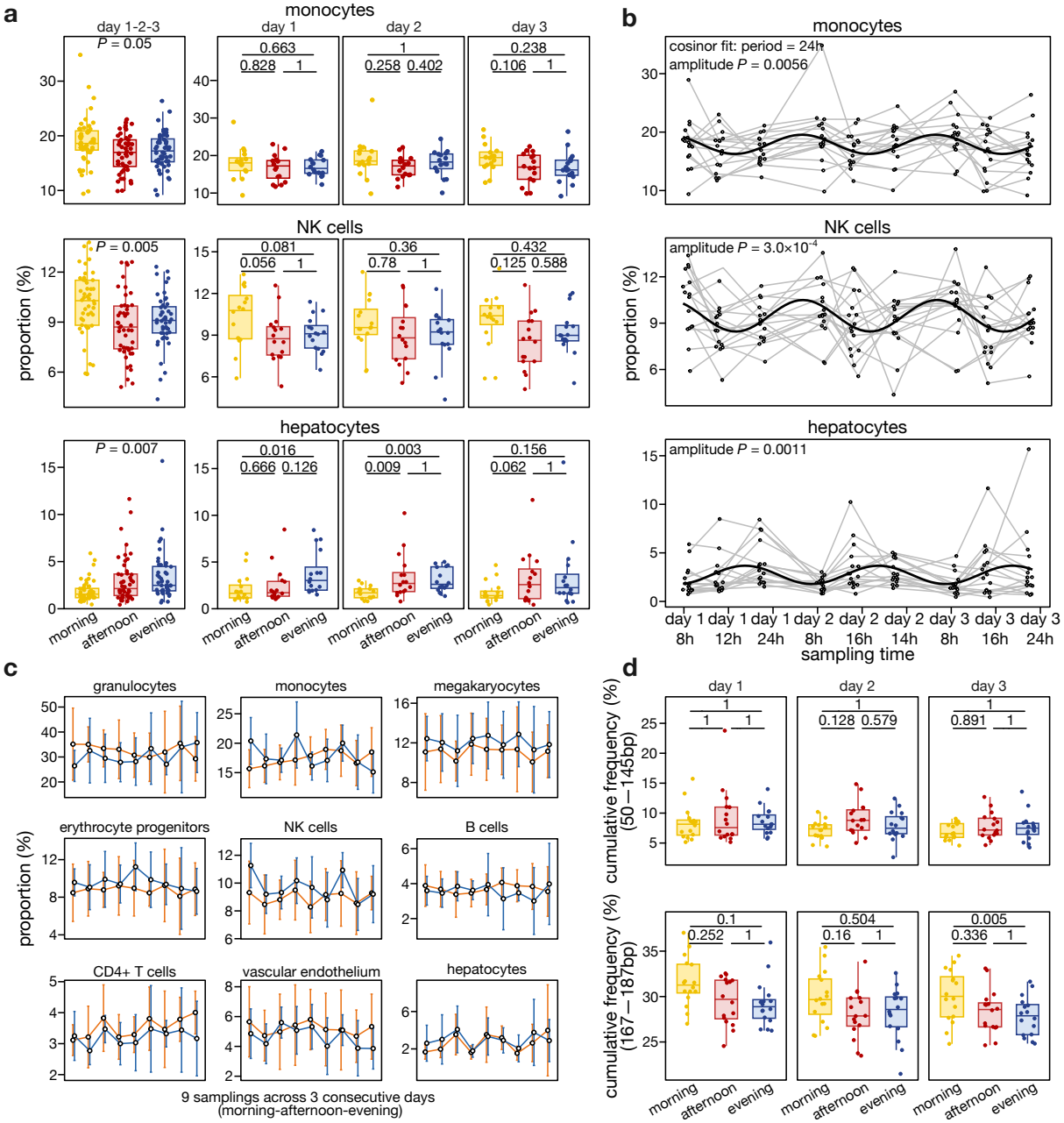


**a,** Diurnal variation in cell type proportions for monocytes (top), NK cells (middle) and hepatocytes (bottom) in samples combined per timepoint (left) and across the three sampling days (right). **b**, Cosinor analysis over a period of 24 hours shows circadian rhythms in cfDNA proportions derived from monocytes (top), NK cells (middle), and hepatocytes (bottom). Solid black lines represent rhythmic fits, while gray lines and symbols depict individual-level changes over time. **c**, Diurnal changes in cell type proportions across all nine sampling time points, shown separately for females (orange) and males (blue). **d**, Cumulative frequency of subnucleosomal (top; 50-145 bp) and mononucleosomal (bottom; 167-187 bp)-sized fragments at different timepoints over three consecutive sampling days. *P* values by repeated measures ANOVA for all sampling days combined, followed by pairwise t-test on each individual day (a, d) and cosinor analysis (b).

**Fig. S3: Demographic factors affecting cfDNA concentration**

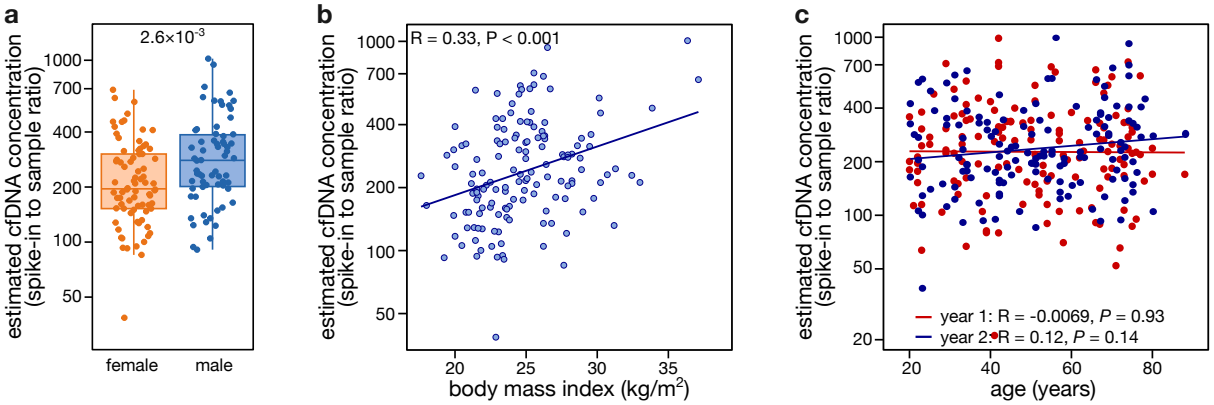


**a**, Comparison of estimated cfDNA concentrations (log10 scaled) between female and male participants in year 2. **b**, Pearson correlation between body mass index and estimated cfDNA concentration (log10 scaled) in year 2. **c**, Pearson correlation between age and estimated cfDNA concentration (log10 scaled) in year 1 (red) and year 2 (blue). *P* value by Wilcoxon rank-sum test (a) or Pearson correlation (b, c).

## Fig. S4: Factors influencing plasma cfDNA composition

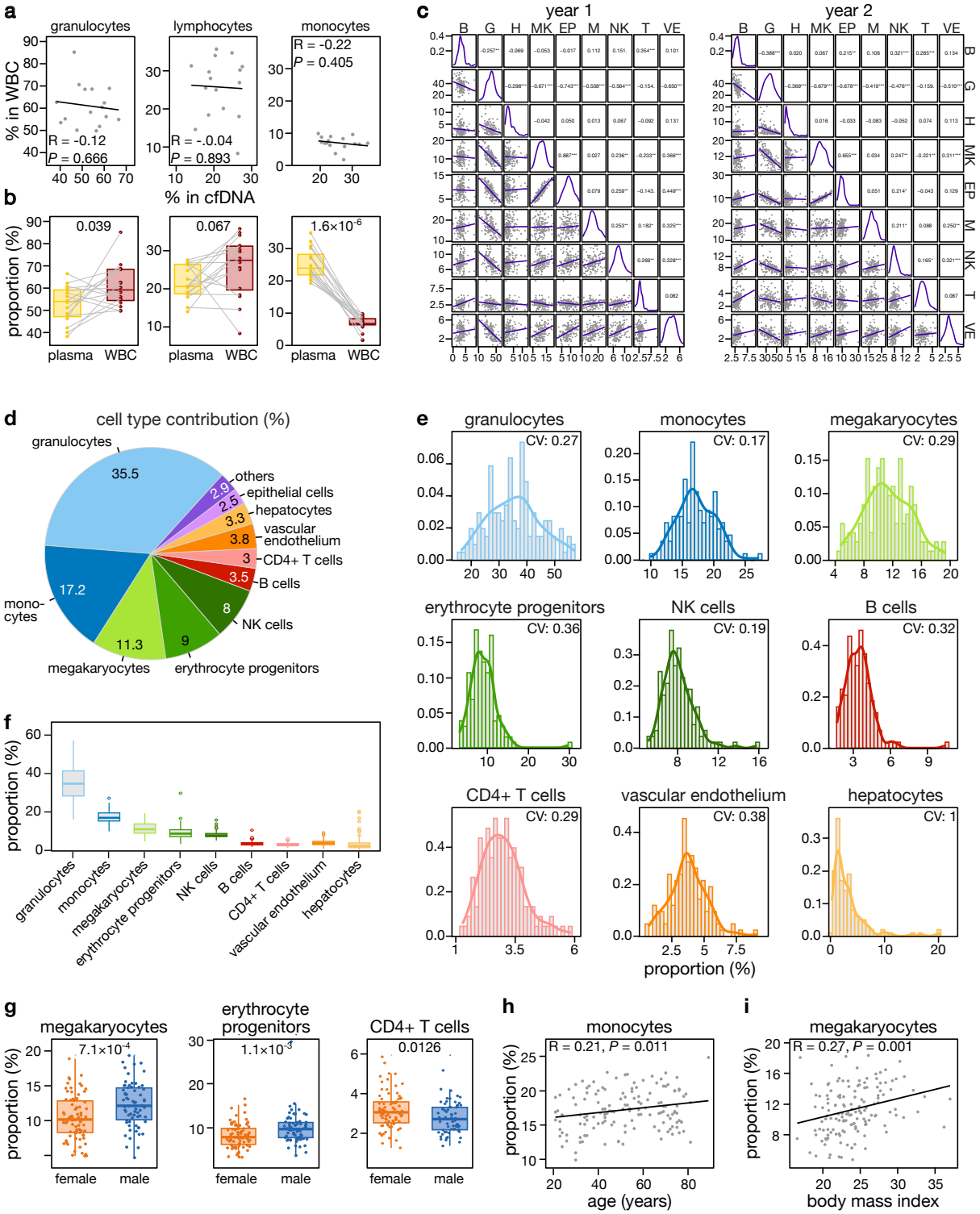


**a**, Pearson correlation between cfDNA-derived white blood cell (WBC) proportions and corresponding cell type proportions in WBCs from whole blood. In whole blood, neutrophil proportions are used as a proxy for granulocytes, given the typically low levels of eosinophils and basophils. **b**, Comparison of cfDNA-derived WBC proportions with matched proportions in WBCs from whole blood. **c**, Pearson correlation between cfDNA fractions for different contributing cell types in year 1 and 2. Significance codes: <0.001 '***', <0.01 '**', <0.01 '*', <0.05 '.', 1 ' '. **d**, Plasma cell type contributions to cfDNA in year 2 samples, represented as

a pie chart. Other cell types include adipocytes, cardiomyocytes, neurons, pancreatic cells, and skeletal muscle cells. **e**, Distribution of proportions (density) for major cell types contributing to plasma cfDNA in year 2. **f**, Interindividual variation in major cell types contributing to plasma cfDNA in year 2. **g**, Comparison of cell type contributions to plasma cfDNA between female and male participants in year 2. **h**, Pearson correlation between monocyte proportions and age in year 2 samples. **i**, Pearson correlation between megakaryocyte proportions and body mass index ($kg/m^2$) year 2 samples. B: B cells; G: granulocytes; H: hepatocytes; MK: megakaryocytes; EP: erythrocyte progenitors, M: monocytes; NK: NK cells; T: CD4+ T cells; VE: vascular endothelium. *P* values by Pearson correlation (a, h, i), paired t-test (b), Pearson correlation (c) or Wilcoxon rank-sum test (g).

**Fig. S5: cfDNA fragmentation patterns in the cross-sectional cohort**

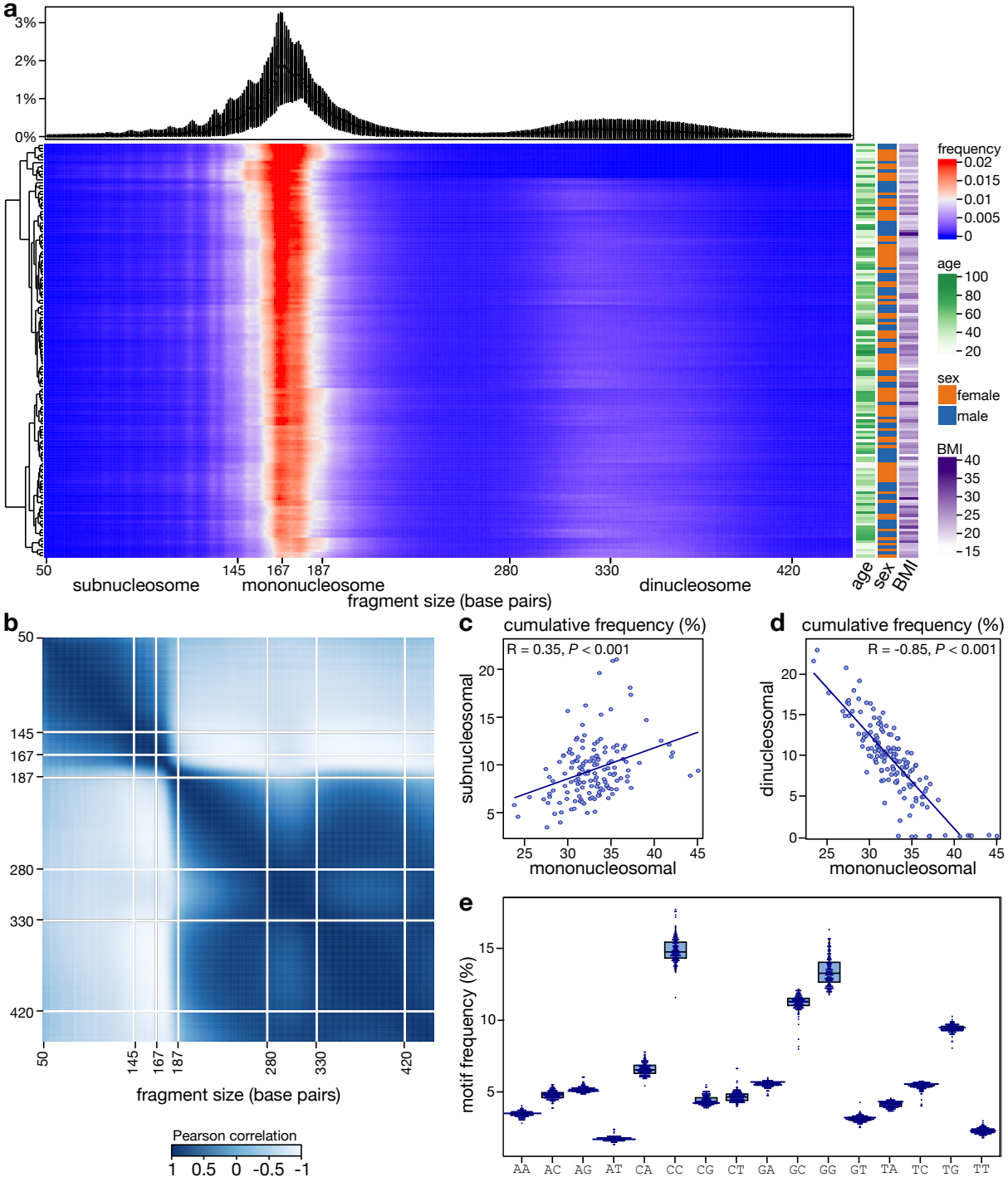


**a**, cfDNA fragment size distributions in year 2 samples, shown as average profiles with error bars representing upper and lower quantiles (top), and a correlation matrix showing associations between fragment sizes and demographic variables (sex, age, and BMI; bottom right). Fragment sizes are defined as subnucleosomal (<145 bp), mononucleosomal (167-187 bp) and dinucleosomal (330-420 bp). **b**, Overview of fragment size correlations in year 2 samples, demonstrating a positive correlation between mononucleosomal and subnucleosomal fragments (**c**), and a negative correlation between mononucleosomal and dinucleosomal fragments (**d**). **e**, Relative contributions of dinucleotide end motifs to plasma cfDNA in year 2 samples. *P* values by Pearson correlation (c, d).

**Fig. S6: Effect of demographic factors and end motif correlations**

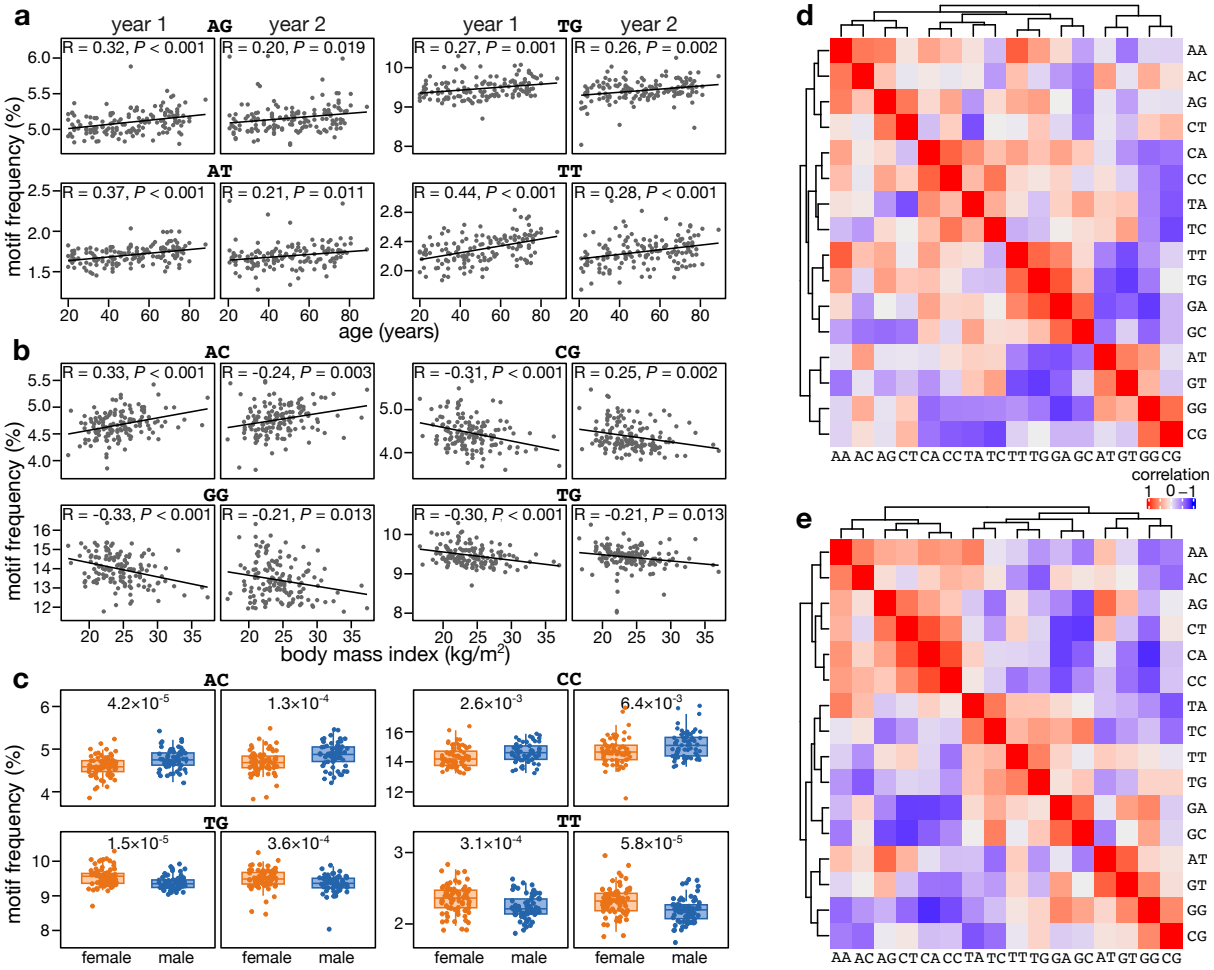


**a-c**, Associations between dinucleotide end motif frequencies and demographic variables in year 1 and year 2 samples. Shown are correlations with age (a), BMI (b) and sex (c). **d**,**e**, Overview of dinucleotide end motif correlations (Pearson) in year 1 (d) and year 2 (e) samples. *P* values by Pearson correlation (a, b), Wilcoxon rank-sum test (c).

**Fig. S7: Factors affecting cfDNA fragmentome characteristics**

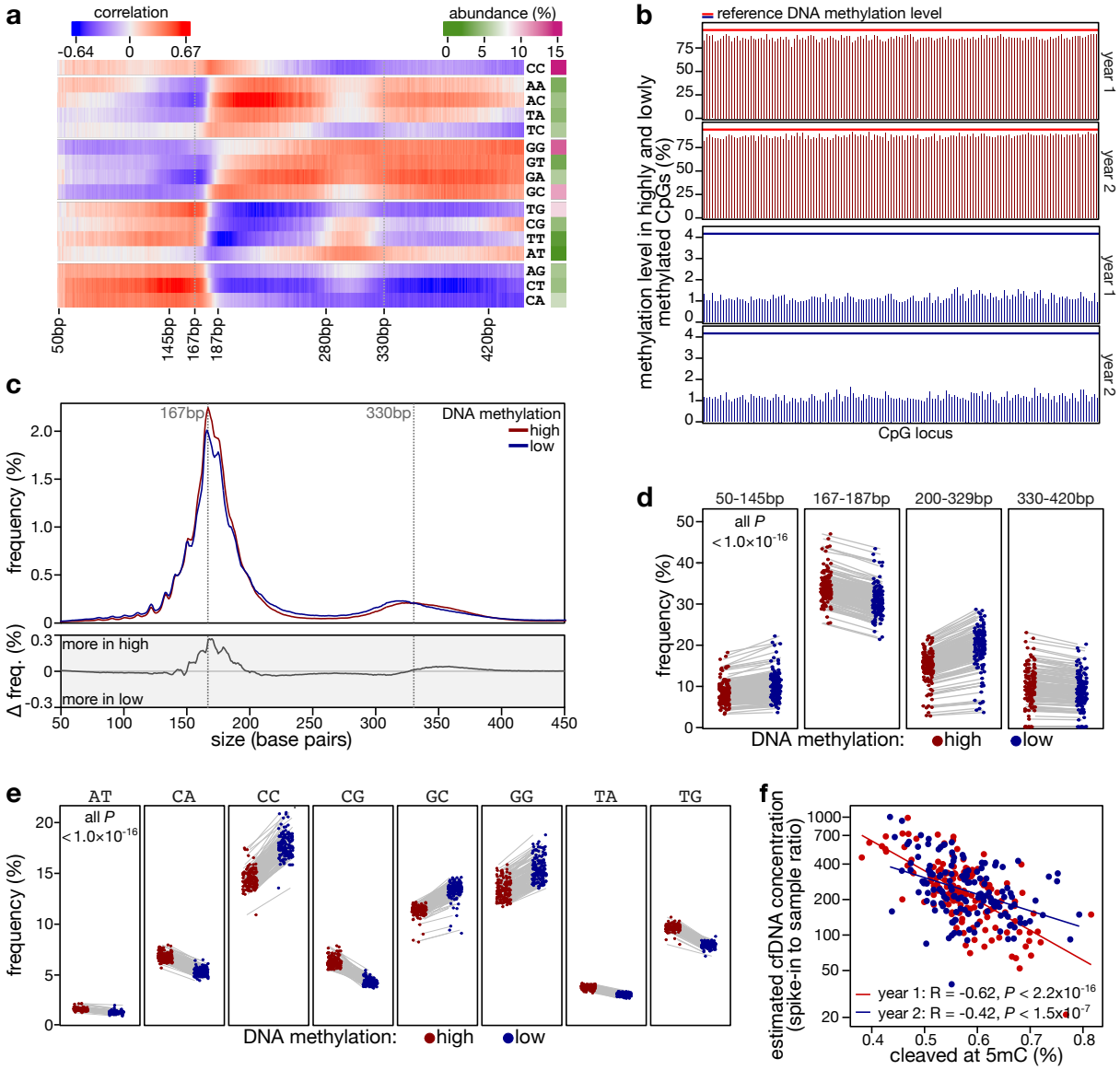


**a**, Spearman correlation matrix showing associations between cfDNA fragment sizes and 2-mer end motifs in year 2 samples, for subnucleosomal (<145 bp), mononucleosomal (167-187 bp), and dinucleosomal fragments (330-420 bp). **b**, CpG loci classified as highly methylated (top, $n$ = 2,953) or lowly methylated (bottom, $n$ = 2,752) across major contributing cell types (see Methods). Reference methylation indicates expected levels at each locus; bars show corresponding methylation levels in cfDNA. **c**, Fragment size distributions (top) and frequency difference (bottom) of cfDNA fragments overlapping the highly and lowly methylated CpGs defined in (b) in year 2 samples. **d**, Cumulative frequency of highly and lowly methylated fragments across different fragment size ranges in year 2 samples. **e**, Frequency of highly and lowly methylated fragments across different 2-mer end motifs in year 2 samples. **f**, Pearson correlation between cleavage at cytosine in CpG context for highly methylated fragments and estimated cfDNA concentration. bp: base pairs. *P* values by paired t-test (d, e) and Pearson correlation (f).

## Fig. S8: Cell-type-specific effects on cfDNA fragmentation

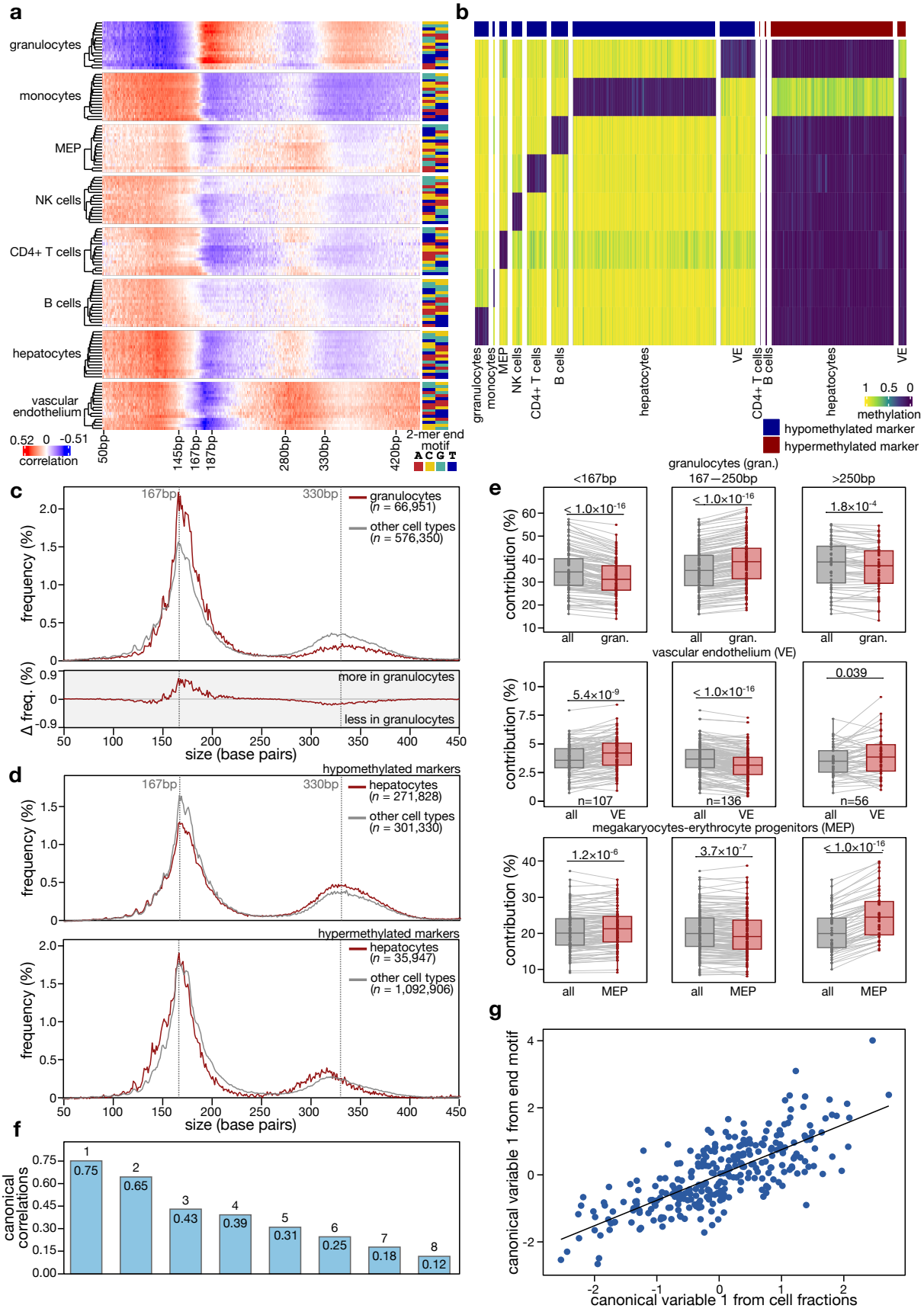


**a**, Spearman correlation matrix showing cell-type specific associations between cfDNA fragment sizes and 2-mer end motifs for major contributing cell types in year 2 samples (*n* =

144). **b**, Heatmap of cell type-specific DNA methylation markers showing at least a 60% difference in average methylation relative to other cell types. **c**, Fragment size distributions (top) and frequency difference (bottom) between hypomethylated granulocyte-specific fragments and all other hypomethylated cell type-specific fragments in year 2 samples. **d**, Fragment size distributions of hypo- and hypermethylated hepatocyte-specific cfDNA fragments (red) compared to those of other cell types (grey) in year 1 samples. **e**, Deconvolution analysis of cfDNA from year 2 samples ($n$ = 144) after *in silico* size selection into three bins (<167 bp, 167–250 bp, >250 bp); samples with <10× coverage per bin were excluded, retaining 107, 136, and 56 samples per bin respectively. **f**, Canonical correlations showing in all canonical dimensions. **g**, Correlation between cfDNA fragmentation patterns and cell type composition along canonical variable 1. *P* values by paired t-test (f).